A theoretical model for the normal contact force of two elastoplastic ellipsoidal bodies

Verena Becker*

Institute For Applied Materials
Karlsruhe Institute of Technology
76344 Eggenstein-Leopoldshafen, Germany
Email: verena.becker@kit.edu

Marc Kamlah

Institute For Applied Materials
Karlsruhe Institute of Technology
76344 Eggenstein-Leopoldshafen, Germany
Email: marc.kamlah@kit.edu

To model the mechanical behavior of granular materials, a reliable description of the material properties is indispensable. Individual grains are usually not perfectly spherical. In batteries, for instance, lithium nickel manganese cobalt oxide (NMC) is a frequently used material, consisting out of particles with possibly ellipsoidal like shapes. As particles may plastically deform under increasing stresses, the paper presents a theoretical model for the normal contact of elastoplastic ellipsoidal bodies for the use in the context of the discrete element method (DEM). The model can be considered as extension of the elastic, elastic-plastic, fully plastic Thornton model by using a more general description to incorporate elliptical contact areas. Further, a formulation for the unloading from elastoplastic loading is derived in such a way, that the contact force is a continuous function of time at the unloading point of the history. All underlying formulae to describe the force-displacement relationship for the static contact problem are derived, partly based on finite element analysis (FEA). To verify the new model, FEAs are performed and their results compared with the model predictions.

Nomenclature

a,b,c	semi-axis of ellipsoid
a_c,b_c	semi-axis of contact ellipse
a_Y,b_Y	semi-axis of contact ellipse at elastic limit
a_p,b_p	semi-axis of contact area with uniform pressure
c_c	equivalent contact radius
c_Y	equivalent contact radius at elastic limit
c_p	equivalent contact radius of contact area with uniform pressure
c_*	maximum equivalent contact radius in history
$c_{\max}$	equivalent contact radius at elastic-plastic limit
e	eccentricity of contact ellipse
E_e,E	(effective) Young's modulus
F_H	elastic Hertzian normal force
F_n	plastic normal force (loading)
$F_{n,\mathrm{UL}}$	plastic normal force (unloading)
F_{pY}	(Hertzian) normal force at elastic limit
f_1,f_2	correction factors
F_0	intersection force with y-axis
$F_{*,H}$	Hertzian force at point of maximum displacement in history
F_{*,p_Y}	plastic normal force at auxiliary point
$F_{*,p_{\max}}$	plastic normal force at point of maximum displacement in history
$\mathbf{K}_{1,2}$	direction of principal curvature
n	constant
m,o,p	constants
s,t,u	constants
p_0	maximum pressure at contact centre
p_Y	maximum pressure at elastic limit
$p_{\max}$	maximum pressure at elastic-plastic limit
$p(x,y)$	pressure distribution across contact area
$\hat{r}$	mean particle radius
R_e	effective contact radius
$R_{e,p}$	effective plastic contact radius
$R_{e,p_{\max}}$	modified effective plastic contact radius
Y	yield stress

α	inclined angle
β	constant
δ_n	displacement in normal direction
δ_Y	displacement at elastic limit
δ_p	permanent plastic displacement
δ_*	maximum displacement in history
$\varepsilon_{\max}$	constant
$\kappa_{1,2}$	principal curvature values
κ_{n,p_Y}	plastic contact stiffness
κ_{H,p_Y}	Hertzian contact stiffness
$\lambda_{\max}$	constant
ν	Poisson's ratio
π	pi
$\sigma_{v,M}$	von Mises equivalent stress

1 Introduction

Granular materials are involved in many industrial or agricultural processes and technical systems. Understanding the motion and the impact of the individual grains is of significant importance to optimize processes and to improve efficiency and performance of systems. The discrete element method (DEM) [1] is a well known and widespread method to simulate large particle structures. In the DEM, the interactions between particles are represented by a virtual overlap (compression) or a gap between the surfaces of particles (tension). The temporal evolution of the motion of an individual particle is gained by numerical integration of the particle's acceleration, which is calculated based on the acting contact forces. For those, an appropriate formulation is necessary to realistically describe the mechanical interactions. At best, the rules are based on the theory of contact mechanics, which incorporates the material properties of the solid particles. These can be determined experimentally, for instance, by performing indentation tests [2]. In addition, Finite-Element-Analyses (FEAs) are an option to provide detailed contact information to develop suitable analytical formulae for the use in the context of the DEM.

The individual contact between two solid bodies is of complex nature. Locally, deformations occur which influence the formation of the contact area and the related contact forces. Even if elastic material behavior is assumed in the beginning, the relationship between force and displacement is usually non-linear. With increasing compression, high stresses can be generated in the particles, which may lead to plastic deformations. Lithium nickel manganese cobalt oxide (NMC), for instance, is a material often used in battery cathodes. Observations and experimental studies showed that NMC particles behave elastically under low levels of compaction, only. Already around 0.1% reduction of their radius, plastic deformations may occur [3]. During the manufacturing of battery electrodes, an essential step is the calendering, in which the electrode is mechanically compressed. As this compression step changes the microstructure, it strongly influences the performance and lifetime of a battery [4–9]. Consequently, the need to correctly describe the mechanical contact in between different grains came up, to be able to determine the overall microstructural properties and to optimize the calendering step.

For the elastic contact, Hertzian theory [10] is well-known. For the plastic contact behavior, various theories exist. Simple models assume a linear relation between the displacement and the resulting contact force [11–14]. However, in experiments, as well as in FEAs it was shown that the real relationship directly after reaching the yield point is still of non-linear nature [15–26] and cannot be sufficiently described by a simple linear model [27].

Mesarovic and Fleck [18, 28] showed that an individual contact passes different regimes during loading. With increasing contact size, the regimes are the elastic regime described by Hertz, an elastic–plastic zone followed by the fully plastic similarity regime and finally the finite deformation regime. The characteristics of the pressure distribution change while passing the different phases, which will be discussed in full detail at the beginning of section **3**.

More complex models, e.g. Thornton [29], Vu-Quoc and Zhang [15] or Martin [30], maintain a non-linear force-displacement relationship to better capture the plastic contact evolution as will be discussed below.

A model for spherical particles differing between an elastic and a plastic phase was developed by Thornton [29, 31]. Thornton divides the evolution of the contact pressure into two phases. At the beginning of the contact evolution, when the contact is still elastic, the parabolic Hertzian contact pressure distribution is valid. This phase is followed by a plastic phase, where the Hertzian pressure is truncated according to a defined pressure limit to account for the observed flattening of the contact pressure distribution [32]. Unloading is assumed to be elastic, including a reduced contact curvature to incorporate the remaining plastic deformations. The model of Martin [30] is equal to the model of Thornton [31], containing adhesion of particles. In [33], Li et al. extend and adapt the theory of Thornton to include the varying curvature during loading, as well as the elastic-plastic transition zone. For the elastic-plastic regime, they use a more detailed pressure distribution function based on FEAs.

Vu-Quoc and Zhang [15] propose a model based on the additive decomposition of the contact radius into an elastic and a plastic part. To take care of the plastic deformations, they correct the contact curvature using an adjustable coefficient. However, a linear relationship for the adjustable coefficient and for the plastic part of the contact radius is assumed, which is not consistent with experiments and observations in FEAs [33].

So far, the afore named analytical models are restricted to spherical shapes only. For ellipsoidal shapes, only few FEAs were performed, e.g. [34, 35]. Theoretical models for the contact of two ellipsoidal bodies exist solely in the context of rough surfaces [36–39]. In these models, an asperity of a rough surface is assumed to consist out of ellipsoidal spots to incorporate the effect of anisotropy. However, most of the models are devoted to the loading situation, only. In

recent developments by Jamari and Schipper [37, 38], complex relations and approximations for the elliptical integrals [40, 41], which appear in the theory of the elliptical contact according to Johnson [42, 43], are applied. The main aim of the developed model is to describe the permanent change of the surface topography as a result of the plastic deformation. Nonetheless, several material parameters need to be identified from experiments to make use of their theory. Beyond that, the focus is set to the loading and the complete unloading stage itself, while the force-displacement relation, especially in the unloading regime is not reported. To know this, is though essential to make use of a model in the context of mechanical DEM. An extensive review concerning investigations on the elastoplastic contact can be found in [44].

In this paper, a theoretical model for the normal contact of two triaxial elastoplastic ellipsoidal bodies is developed extending the theory of [31] with the help of FEAs. The formulae to describe the force-displacement relationship in the static contact problem are derived and presented. Lastly, the theory is validated by comparing the model predictions with the results of FEAs. Special attention is paid to a reliable description of the force-displacement connection to finally incorporate the new model in the context of mechanical DEM.

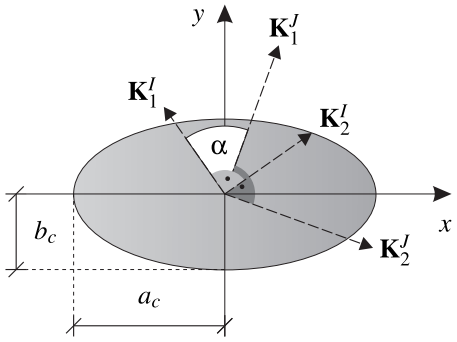

Fig. 1. Elliptical contact area of two ellipsoidal bodies with the semi-axes a_c, b_c, the principal curvature directions $\mathbf{K}_{1,2}^{I,J}$ and the angle of inclination α

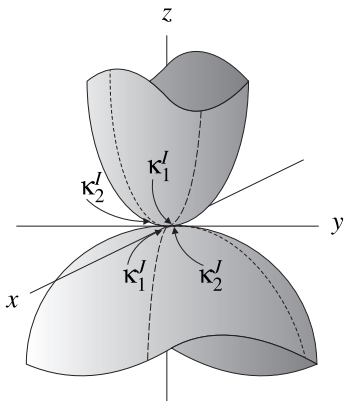

Fig. 2. Contact geometry of two ellipsoidal bodies with the principal curvatures $\kappa_{1,2}^{I,J}$

2 Hertz theory of elastic contact

Consider the contact interaction between two elastoplastic ellipsoidal bodies I and J. Use of the von Mises stress $\sigma_{v,M}$ distinguishes two overall zones. If the equivalent stress $\sigma_{v,M}$ in the particle produced by the contact force F_H stays below the yield strength of the material in simple tension Y, the contact behavior is purely elastic. In this case the situation is describable with the established Hertz theory [10, 42]. In Hertz theory, when loaded in normal direction, the two solids will deform and touch each other at an elliptical region. Hertz links the real deformation of the contact zone to the virtual overlap δ_n of the two bodies. The Hertzian pressure distribution $p(x,y)$ along the elliptical contact surface has the parabolic profile

$$p(x,y) = p_0 \left[1 - \left(\frac{x}{a_c} \right)^2 - \left(\frac{y}{b_c} \right)^2 \right]^{1/2} \quad . \tag{1}$$

The maximum contact pressure p_0 occurs at the center of the contact ellipse, which has the major and minor semi-axes a_c and b_c, cf. Fig. 1. The variable $c_c^2 = a_c b_c$ is the so-called equivalent contact radius, which would produce a circle of the same size as the area of the contact ellipse. For the special case of two spheres, the ellipse reduces to a circle with $a_c = b_c = c_c$. $\mathbf{K}_1^I, \mathbf{K}_2^I$ and $\mathbf{K}_1^J, \mathbf{K}_2^J$ are the two systems of the principal curvatures, which do not have to coincide with each other. In general, they are twisted by the angle of inclination α, cf. Fig. 1. Further, for any position at the surface of a particle, its two principal curvatures are perpendicular to each other.

For the definition of the effective contact radius R_e, it is important to provide a detailed description of the geometry in the contact point. Hertz theory applies only on condition that the surfaces of the contacting solids are continuous and the contact deformation induced is significantly smaller than the size of each solid. The contact problem remains of localized nature and the small deformed contact regions thus may be approximated as quadric curved surfaces. To describe the contact geometry, the two principal curvatures of each solid, $\kappa_1^I, \kappa_2^I, \kappa_1^J$ and κ_2^J, at the contact point are of interest, cf. Fig. 2. They crucially influence the arising contact force regardless of the overall shape of each solid. Considering non-spherical particles, the calculation of the principal curvature is not trivial. According to Appendix **A** and in detail explained in [45], the principal curvature of an ellipsoid can be determined. The maximum contact pressure p_0 is defined as

$$p_0 = \frac{2E_e c_c}{\pi R_e f_1^3} \quad , \tag{2}$$

where the effective Young's modulus E_e

$$E_e = \left(\frac{1-\nu^{I2}}{E^I} + \frac{1-\nu^{J2}}{E^J} \right)^{-1} \quad , \tag{3}$$

depends on the Young's modules E^k of the material of each particle and their Poisson's ratio ν^k, $k = I,J$. To capture the ellipticity of the contact area, so-called correction factors f_1 and f_2 are introduced. They fit the elliptical integrals appearing in the expression for the eccentricity of the contact ellipse [43]. Due to their simple formulation, f_1 and f_2 are sufficient for typical geometries in terms of precision and therefore more suitable for practical purposes. The correction factors gradually decrease from a value of one as the contact becomes more elliptical. The approximated functions according to [43] are

$$\begin{aligned} f_1 &\approx 1 - \left[\left(\frac{A}{B} \right)^{0.0602} \right]^{1.456} \quad , \\ f_2 &\approx 1 - \left[\left(\frac{A}{B} \right)^{0.0684} \right]^{1.531} \quad . \end{aligned} \tag{4}$$

Given the principal curvatures and the inclination angle α, cf. Appendix **A**, the variables A and B in Eqn. (4) can be determined [42] as

$$\begin{aligned} A+B =& \frac{1}{2} \left[\kappa_1^I + \kappa_2^I + \kappa_1^I + \kappa_2^I \right] \quad , \\ B-A =& \frac{1}{2} \Big[\left(\kappa_1^I - \kappa_2^I \right)^2 + \left(\kappa_1^I - \kappa_2^I \right)^2 \\ & + 2 \left(\kappa_1^I - \kappa_2^I \right) \left(\kappa_1^I - \kappa_2^I \right) \cos(2\alpha) \Big]^{1/2} \quad . \end{aligned} \tag{5}$$

With these values the effective contact radius

$$R_e = \frac{1}{2} \frac{1}{\sqrt{AB}} \quad , \tag{6}$$

the eccentricity

$$e^2 = 1 - \left(\frac{b_c}{a_c} \right)^2 \approx 1 - \left(\frac{A}{B} \right)^{4/3} \tag{7}$$

and the major and minor semi-axes

$$a_c = c_c \left(1 - e^2 \right)^{-1/4} , \quad b_c = c_c \left(1 - e^2 \right)^{1/4} \tag{8}$$

are identified. The effective contact radius and the virtual overlap δ_n are related by

$$\delta_n = \frac{a_c b_c}{R_e} \frac{f_2}{f_1^2} = \frac{c_c^2}{R_e} \frac{f_2}{f_1^2} \quad . \tag{9}$$

Finally, the elastic contact force F_H is obtained by the integration of the contact pressure $p(x,y)$ over the contact area $A_c = \pi a_c b_c$ as

$$F_H = \frac{4}{3} E_e \sqrt{R_e} {\delta_n}^{3/2} f_2^{-3/2} \quad . \tag{10}$$

3 Theory of elastoplastic contact

Already since the early 1950's, experiments on the normal indentation of an elastoplastic half-space by a rigid sphere were performed [32]. The findings were later confirmed by FEAs, cf. [17–24]. All results, ours in section **4** included, show the same behavior.

Under normal compression until a maximum pressure value of about $p_0 = p_Y = 1.6Y$, the contact behaves purely elastic and the pressure distribution is Hertzian [17, 42]. In the subsequent elastic-plastic regime, small plastic deformations occur under the contact surface, which are captured by an elastic deformation of the neighbouring solid material. Once the threshold p_Y is exceeded, a localized plastic deformation zone spreads out and finally reaches the contact surface [42]. This process is accompanied by a significant change in the pressure distribution. The increase of the maximum contact pressure slows down until an almost constant value of the contact pressure over an enlarging area around the center of the contact ellipse is reached. We call this phase elastic-plastic transition regime.

If the maximum pressure during the indentation of a sphere reaches a value of about three times the yield stress Y [17, 32, 42], the pressure distribution is completely flattened and the so-called fully plastic similarity regime begins. Further increase of the normal contact force leads to the enlargement of the contact ellipse, only. The maximum pressure does not rise further. For ellipsoidal particles, the limiting value of the maximum pressure depends not only on the material, but on the geometry of the particles as well, which will be shown in section **4**.

Finally, for large deformations, represented by huge virtual overlaps, finite deformations will dominate the contact behavior and plastic deformations extend beyond the contact area [46]. The findings in [18] and [47] show that the finite deformation regime is entered for a ratio of $c_c/\hat{r} = 0.16..0.4$ for the equivalent contact radius c_c and the mean particle radius $\hat{r}$. Such large deformations are beyond the scope of the here developed theory.

Thornton [29, 31] was the first, who suggested to split the contact pressure distribution into an elastic and a plastic part. In the elastic regime, the pressure distribution follows the Hertzian profile, while in the plastic phase, the Hertzian pressure distribution is truncated to describe the arising flattening of the pressure profile. Further in [33], the

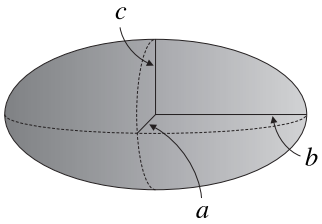

Fig. 3. Geometry of an ellispoid with the semi-axes a, b and c

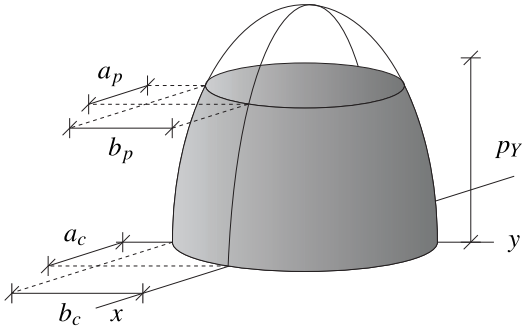

Fig. 4. Plastic contact pressure distribution in normal direction with the yield pressure p_Y, the semi-axes of the contact area a_c, b_c and the semi-axes of the contact area at yield pressure a_p, b_p

initially elastic-fully plastic model was extended to capture the elastic-plastic transition regime.

In this work, we pursue the approach of Thornton with a variation of the elastic-plastic phase and the unloading regime to incorporate ellipsoidal geometries. Hertzian theory is assumed to be valid until the elastic limit is reached. In the elastic-plastic and fully plastic phase, a truncated Hertzian pressure distribution is presumed. Consequently, the contact curvature in the here developed theory does not change during loading and is determined by Eqn. (6) from the undeformed particle geometries. During unloading, Hertzian theory is assumed to be valid again, but a reduced plastic curvature is taken into account, as well as a changed unloading overlap to incorporate the changes in the contact curvature due to permanent plastic deformations. Below, all necessary formulae for the different regimes - elastic-plastic loading, fully plastic loading, as well as the unloading stage - are derived and discussed in detail.

3.1 Plastic contact for an ellipsoid

An ellipsoid is described in local coordinates by the implicit function

$$\left(\frac{x}{a}\right)^2 + \left(\frac{y}{b}\right)^2 + \left(\frac{z}{c}\right)^2 = 1 \quad , \tag{11}$$

where a, b and c are the three semi-axes, cf. Fig. 3. Once the elastic limit $p_0 = p_Y$ is reached, the plastic contact force

$$F_n = F_H - \int_0^{b_p}\int_0^{a_p} \left[p\left(x,y\right) - p_Y\right] \mathrm{d}x\mathrm{d}y \tag{12}$$

is determined by the difference of the elastic contact force F_H, which would result in the same contact area $A_c = \pi a_c b_c$, less the elastic cap, which exceeds the yield criterion p_Y, cf. Fig. 4. The variables a_p and b_p are the semi-axes of the cross sectional area at the plastic plateau, over which a uniform contact pressure is assumed. To formulate an appropriate theory for ellipsoidal particles, we introduce the transformation of cartesian coordinates into polar coordinates first

$$\begin{aligned}
&\phi(r,\varphi) = \begin{bmatrix} a_p r\cos\varphi \\ b_p r\sin\varphi \end{bmatrix}, \\
&\frac{\partial\phi}{\partial\left(r,\varphi\right)} = \begin{bmatrix} a_p\cos\varphi & -a_p r\sin\varphi \\ b_p\sin\varphi & b_p r\cos\varphi \end{bmatrix} \quad , \\
&\det\left|\frac{\partial\phi}{\partial\left(r,\varphi\right)}\right| = a_p b_p r \quad , \\
&r\in[0,1]\,, \quad \varphi\in[0,\pi/2] \quad .
\end{aligned} \tag{13}$$

Application of the transformation in Eqn. (13) to Eqn. (12) results in

$$F_n = F_H - 4\int_0^1\int_0^{\pi/2} \left[p\left(r,\varphi\right) - p_Y\right] a_p b_p r \,\mathrm{d}\varphi\mathrm{d}r \quad . \tag{14}$$

With the relation in Eqn. (1), it follows

$$\begin{aligned}
F_n = {} & \pi a_p b_p p_Y + F_H - 4p_0 \\
& \int_0^1\int_0^{\pi/2} \sqrt{1 - \left(\frac{a_p r\cos\varphi}{a_c}\right)^2 - \left(\frac{b_p r\sin\varphi}{b_c}\right)^2}\, a_p b_p r\,\mathrm{d}\varphi\mathrm{d}r \quad .
\end{aligned} \tag{15}$$

Due to the flattening of the contact pressure in the plastic regime in parallel to the contact area, we assume that the ratio of the contact semi-axes a_c/b_c and the semi-axes at the plateau a_p/b_p is the same, which gives

$$\frac{a_p}{a_c} = \frac{b_p}{b_c} = \frac{c_p}{c_c} \quad , \tag{16}$$

where c_p is the equivalent contact radius of the contact area with uniform pressure. Insertion of Eqn. (16) into Eqn. (14)

leads to

$$F_n = \pi a_p b_p p_Y + F_H - 2\pi p_0 a_p b_p \int_0^1 \sqrt{1-\left(\frac{c_p}{c_c}\right)^2 r^2}\, r\,\mathrm{d}r \quad . \tag{17}$$

Rewriting of Eqn. (17) as

$$F_n = \pi a_p b_p p_Y + F_H - 2\pi p_0 a_p b_p \int_0^1 \sqrt{1-\left(\frac{c_p}{c_c}\right)^2 r^2}\cdot\frac{2}{2}\cdot(-1)^2\cdot\left(\frac{c_p c_c}{c_p c_c}\right)^2 r\,\mathrm{d}r \quad , \tag{18}$$

and making use of the integration rule

$$\int (u(x))^n \cdot u'(x)\,\mathrm{d}x = \frac{1}{n+1}(u(x))^{n+1} \quad , \tag{19}$$

gives us in combination with Eqn. (2)

$$F_n = \pi a_p b_p p_Y + F_H \left[1-\left(\frac{c_p}{c_c}\right)^2\right]^{3/2} \quad . \tag{20}$$

As a second condition, according to Fig. 4, the yield contact pressure p_Y has to correspond to the elastic contact pressure $p(x,y)$, when $x = a_p \cos\varphi$ and $y = b_p \sin\varphi$, which gives

$$p_Y = \frac{3F_H}{2\pi a_c b_c}\left[1-\left(\frac{c_p}{c_c}\right)^2\right]^{1/2} \quad . \tag{21}$$

With the use of Eqn. (9) this leads to the relation

$$\frac{c_Y^2}{c_c^2} = \left[1-\left(\frac{c_p}{c_c}\right)^2\right] \quad , \tag{22}$$

which can be simplified to

$$c_c^2 = c_Y^2 + c_p^2 \tag{23}$$

and where c_Y is the equivalent contact radius at the elastic limit. Finally, insertion of Eqn. (23) into Eqn. (20) gives the generalized Thornton type normal force formulation in the plastic regime for the contact of ellipsoidal bodies:

$$\boxed{F_n = \pi p_Y \left(c_c^2 - c_Y^2\right) + F_{p_Y}} \tag{24}$$

3.2 Elastic-plastic zone

In reality, the material behavior is not perfectly elastic - fully plastic, but involves different phases. Thus, the contact behavior is described by the Hertzian theory until the elastic limit $p_0 = p_Y = 1.6Y$ is reached for the first time. At that point, the contact enters the elastic-plastic regime. During the elastic-plastic transformation phase, the maximum contact pressure increases further, but slower, up to a second threshold $p_0 = p_{\max} = \lambda_{\max} Y$ [42]. While the maximum contact pressure increases and the pressure profile flattens, the equivalent contact radius grows from the value c_Y at the elastic limit to a value $c_{\max} = \varepsilon_{\max} c_Y$, when the maximum contact pressure reaches $p_{\max}$. The exact values for both maximum ratios $\lambda_{\max}$ and $\varepsilon_{\max}$ are material and geometry dependent. The current value of $1.6 \le \lambda \le \lambda_{\max}$ in the elastic-plastic regime varies conditional on the changes of the current overlap and must increase only. In our model, λ depends on the curvature in the contact point to incorporate the influence of the eccentricity of the contact ellipse and of the non-sphericity of the particle shape. In the elastic-plastic regime, the force-displacement curve we now employ follows the relation

$$F_n = \pi p_\lambda \left(c_c^2 - c_Y^2\right) + F_{p_Y}\,, \quad p_Y \le p_\lambda \le p_{\max} \quad , \tag{25}$$

but with

$$p_\lambda = \lambda Y \quad . \tag{26}$$

Although it is indicated in [42], that the normal contact pressure varies with the contact radius, there is no exact solution reported. Thus, in the present model we refer to the relation for spheres in [33]. Extending a relation given there with the help of the equivalent contact radius at the elastic limit c_Y and the equivalent contact radius c_c to ellipsoidal shapes, we assume the relationship

$$p_\lambda = \lambda_{\max} Y - (\lambda_{\max} - 1.6)\, Y \left[\frac{\varepsilon_{\max} c_Y - c_c}{(\varepsilon_{\max} - 1) c_Y}\right]^n \quad . \tag{27}$$

If Eqn. (27) is divided by Y, the formula for λ

$$\lambda = \lambda_{\max} - (\lambda_{\max} - 1.6)\left[\frac{\varepsilon_{\max} c_Y - c_c}{(\varepsilon_{\max} - 1) c_Y}\right]^n \tag{28}$$

results. Given the fit parameters $\lambda_{\max}$, $\varepsilon_{\max}$ and n, as well as the equivalent contact radius at the yield point c_Y, the current value of λ is calculated from Eqn. (28) as a function of the current equivalent contact radius c_c, which is again a function of the overlap through Eqn. (9). This relation remains valid until c_c reaches the maximum value defined by

$$c_Y \le c_c \le c_{\max} = \varepsilon_{\max} c_Y \quad . \tag{29}$$

The maximum value $c_{\max}$ is exactly reached, when the maximum pressure reaches $p_{\max} = \lambda_{\max} Y$ for the first time. The corresponding overlap at the elastic-plastic limit, when $c_c = c_{\max}$ and $p_0 = p_{\max}$, is

$$\delta_{\max} = \frac{c_{\max}^2}{R_e} \frac{f_2}{f_1^2} \quad . \tag{30}$$

The parameters $\lambda_{\max}$ and $\varepsilon_{\max}$, as well as the exponent n are chosen to match the exact profile of λ, obtained from FEAs, cf. section **4**. To take into account the particle shape and thus the ellipticity of the contact area, $\lambda_{\max}$ and $\varepsilon_{\max}$ are assumed to depend on the principal curvatures $\kappa_1^I, \kappa_1^J, \kappa_2^I, \kappa_2^J$ in the contact point of both particles through the dependence on the effective contact radius R_e. Details on these fit functions will be given in section **4**.

3.3 Fully plastic zone

If the overlap is larger than $\delta_{\max}$ in Eqn. (30), the fully plastic similarity zone is entered. The maximum contact pressure p_0 stays from now on at the maximum value of $p_{\max} = \lambda_{\max} Y$ and does not increase further. The force-displacement relation is then

$$F_n = \pi p_{\max} \left(c_c^2 - c_Y^2 \right) + F_{pY} \quad , \tag{31}$$

which results in a linear rising behavior.

3.4 Unloading

As mentioned before, we neglect possible changing of the curvature during elastic-plastic and fully plastic loading, meaning that the curvature stays equal to $1/R_e$ as determined by Eqn. (6) from the undeformed particle geometries. We now assume, following [31], that unloading from any point is purely elastic and thus follows Hertzian theory. However, due to the remaining deformation, it is performed with some yet to be determined reduced plastic contact curvature $1/R_{e,p}$, which is smaller than the initial contact curvature $1/R_e$ of the particle in the contact point. As further quantities we introduce the ever occurred maximum displacement δ_* and the corresponding ever occurred maximum equivalent contact radius c_*.

As a first step in motivating our theory, we neglect the elastic-plastic regime for the time being. This means that the theory is considered to be elastic - fully plastic, only. This situation is visualized in Fig. 5. Due to the occurring plastic deformations during the fully plastic regime, a permanent plastic overlap δ_p remains after complete unloading, which can be seen in Fig. 5 at the end of the orange dashed unloading path at point E. Thus, as only the elastic part of the deformation will recover, we consider during unloading the overlap

$$\delta_{\mathrm{UL}} = \delta_n - \delta_p \quad , \tag{32}$$

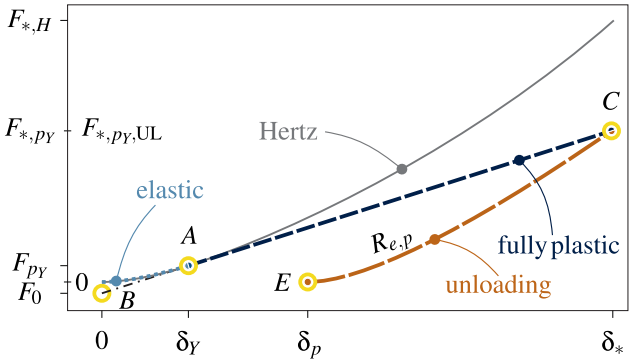

Fig. 5. Elastic - fully plastic theory according to [29]: contact force vs. displacement

which results as the difference between the current overlap δ_n and the remaining plastic overlap δ_p. In the maximum point at the end of fully plastic loading, the contact area πc_*^2, which would be reached in the fully plastic contact, has to be equal to the contact area at the beginning of unloading $A_{*,\mathrm{UL}}$, to ensure continuity of the contact area at this point of the history. This gives the condition

$$\pi c_*^2 = A_{*,\mathrm{UL}} \quad . \tag{33}$$

Rewriting and making use of the relation given in Eqn. (9),

$$\begin{aligned} {c_*}^2 = R_e \delta^* \frac{f_1^2}{f_2} &= \underbrace{R_{e,p} \left(\delta_* - \delta_p \right) \frac{f_1^2}{f_2}}_{\frac{A_{*,\mathrm{UL}}}{\pi}} \\ \rightarrow \quad \delta_p &= \delta_* \left(1.0 - \frac{R_e}{R_{e,p}} \right) \quad , \end{aligned} \tag{34}$$

results in the relationship between the maximum ever occurred overlap δ_* and the plastic overlap δ_p.

After reaching the yield point, point A in Fig. 5, the force increases linearly in the fully plastic regime. For the maximum overlap δ_*, ever experienced in the contact history, the corresponding contact force is, according to Eqn. (24), $F_{*,pY} = \pi p_Y \left(c_*^2 - c_Y^2 \right) + F_{pY}$. We call this point first auxiliary point, which is labeled as C in Fig. 5.

To determine $R_{e,p}$, further conditions are necessary. Taking the derivative of the fully plastic contact force formulation in Eqn. (24) with respect to the normal overlap δ_n, leads to the plastic contact stiffness $k_{n,pY}$. At the elastic limit, point A in Fig. 5, where $p_0 = p_Y$ and $\delta_n = \delta_Y$, the plastic contact stiffness corresponds with the elastic stiffness $k_{H,pY}$ according to the Hertzian theory giving

$$\underbrace{\pi R_e \frac{f_1^2}{f_2} p_Y}_{k_{n,pY}} = \underbrace{\frac{2 E_e \sqrt{R_e} \sqrt{\delta_Y}}{f_2^{3/2}}}_{k_{H,pY}} \quad . \tag{35}$$

Details concerning the calculation and derivation of Eqn. (35) are given in Appendix **B**. In accordance with [31], a linear tangential extension of the fully plastic force-displacement curve from the elastic limit δ_Y to a vanishing overlap of $\delta_n = 0$, gives the point of intersection with the y-axis $F_0 < 0$. This point is the second auxiliary point, which is labeled as B in Fig. 5. Due to the linear extension, the difference quotient, build up with the information at the elastic limit and the information at point B, has to correspond to the contact stiffness in Eqn. (35)

$$k_{n,p_Y} = k_{H,p_Y} = \frac{F_{p_Y} - F_0}{\delta_Y - 0} \quad . \tag{36}$$

The same operation is performed with the information at point B and the information of the first auxiliary point C. It follows

$$k_{H,p_Y} = k_{n,p_Y} = \frac{F_{*,p_Y} - F_0}{\delta_* - 0} \quad . \tag{37}$$

Reformulation of Eqn. (36) together with Eqn. (35) gives the condition

$$\begin{aligned} F_0 &= F_{p_Y} - \underbrace{\frac{3}{2} \cdot \frac{2}{3} \cdot \frac{\overbrace{2E_e\sqrt{R_e}\sqrt{\delta_Y}}^{k_{H,p_Y}}}{f_2^{3/2}} \cdot \delta_Y}_{F_{p_Y}} \\ &= -\frac{1}{2} F_{p_Y} \quad . \end{aligned} \tag{38}$$

Solving Eqn. (37) with respect to δ_* and making use of Eqn. (38) and the relation in Eqn. (9) results in

$$\begin{aligned} \underbrace{\delta_* \cdot R_e \frac{f_1^2}{f_2}}_{c_*^2} \pi p_Y &= F_{*,p_Y} + 0.5 F_{p_Y} \quad , \\ c_*^2 &= \frac{F_{*,p_Y} + 0.5 F_{p_Y}}{\pi p_Y} \quad . \end{aligned} \tag{39}$$

At point C, the unloading force $F_{*,p_Y,\mathrm{UL}}$ is equal to the force F_{*,p_Y} at the end of fully plastic loading to ensure continuity of the contact force, which leads to the condition

$$F_{*,p_Y,\mathrm{UL}} = F_{*,p_Y} \quad . \tag{40}$$

If the contact would have deformed purely elastic, the corresponding elastic force $F_{*,H}$ at δ_* would be calculated by the Hertzian theory, see Fig. 5 and Eqn. (10). Assuming that unloading is elastic, the contact force during unloading can be calculated from Eqn. (10) based on δ_{UL}, cf. Eqn. (32). Furthermore, the yet unknown reduced plastic contact curvature $1/R_{e,p}$ is presumed to incorporate the occurring permanent plastic deformations. Based on these two assumptions and Eqn. (10), the relationship for the unloading regime is then

$$\begin{aligned} F_{n,p_Y,\mathrm{UL}} &= \frac{4}{3} E_e \sqrt{R_{e,p}} \left(\delta_n - \delta_p\right)^{3/2} f_2^{-3/2}, \quad \delta_n \geq \delta_p \\ F_{n,p_Y,\mathrm{UL}} &= 0, \qquad\qquad\qquad\qquad\quad \delta_n < \delta_p \quad . \end{aligned} \tag{41}$$

Insertion of Eqn. (34) in Eqn. (41) leads to

$$F_{n,p_Y,\mathrm{UL}} = \frac{4}{3} E_e \sqrt{R_{e,p}} \left(\delta_n \frac{R_e}{R_{e,p}}\right)^{3/2} f_2^{-3/2} \quad . \tag{42}$$

For the maximum point C, where $\delta_n = \delta_*$, reformulation of Eqn. (42) gives with the help of Eqn. (9)

$$F_{*,p_Y,\mathrm{UL}} R_{e,p} = F_{*,H} R_e \quad . \tag{43}$$

Thus, rewriting of Eqn. (43) and making use of Eqn. (39), as well as the relation in Eqn. (9), leads to the formula for the reduced effective plastic contact radius

$$\begin{aligned} R_{e,p} &= \frac{F_{*,H} R_e}{F_{*,p_Y}} \\ &= \frac{1}{F_{*,p_Y}} \frac{4}{3} E_e \underbrace{\sqrt{R_e} \delta_*^{3/2} f_2^{-3/2} \cdot R_e}_{\left(c_*^2/f_1^2\right)^{3/2}} \\ &= \frac{4E_e}{3F_{*,p_Y}} \left(\frac{F_{*,p_Y} + 0.5F_{p_Y}}{\pi p_Y}\right)^{3/2} \frac{1}{f_1^3} \quad . \end{aligned} \tag{44}$$

With the reduced curvature, the plastic part of the overlap can be determined according to Eqn. (34). Subsequently, the contact force $F_{*,p_Y,\mathrm{UL}}$ during unloading can be calculated from Eqn. (41).

So far, the afore derived relations do only describe unloading for an elastic - fully plastic theory, where the elastic-plastic transition regime is neglected. To incorporate the transition phase, attention has to be paid to the fact that the maximum pressure after exceeding the elastic limit at $p_0 = p_Y$ increases further, until reaching the elastic-plastic limit, when $p_0 = p_{\max}$. In Fig. 6, a symbolic load displacement trajectory of the elastic-plastic and fully plastic loading of the theory to be developed within this work is shown as bold blue line from point A to point D. Again the elastic - fully plastic theory according to [29] from Fig. 5 is shown as thin line with the fully plastic loading from point A to point C and the unloading regime from point C to point E. As can be seen by comparing the path from point A to D with the path from point A to C, the force-displacement relation in the elastic-plastic regime is still non-linear, because of the stiffnes still increasing during this regime. This leads

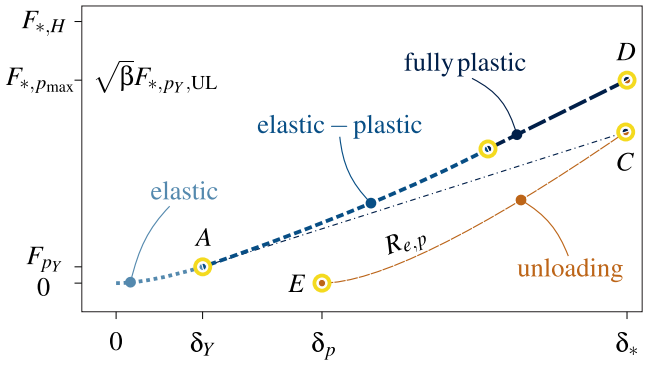

Fig. 6. Elastic - elastic-plastic - fully plastic theory (bold lines) vs. elastic - fully plastic theory [29] (thin lines): contact force vs. displacement

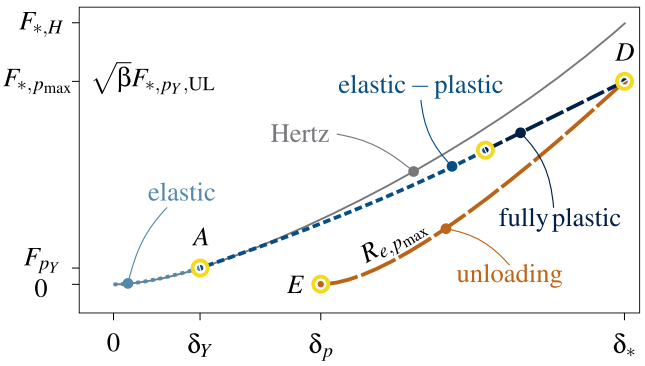

Fig. 7. Elastic - elastic-plastic - fully plastic theory including the unloading regime: contact force vs. displacement

to a higher maximum force $F_{*,p_{\max}}$ at a certain value of the maximum ever occurred overlap δ_*, labeled as point D in Fig. 6. At this point, it has to be emphasized that continuity of the contact force as a function of time is an important feature to ensure stability of DEM simulations. Thus, to ensure continuity of the contact force in point D at unloading, the condition in Eqn. (40) has to be adjusted. To this end, we reformulate Eqn. (40) with some factor beta such that it reads

$$\beta F_{*,p_Y,\mathrm{UL}} = F_{*,p_{\max}} \quad . \tag{45}$$

This factor has the effect to shift the force at point C in Fig. 6 to point D, without changing the permanent plastic displacement δ_p at point E. Solving Eqn. (45) for β and making use of Eqn. (31) and Eqn. (25), the value of β is obtained as

$$\beta = \frac{\pi p_\lambda \left(c_*^2 - c_Y^2\right) + F_{p_Y}}{\frac{4}{3} E_e \sqrt{R_{e,p}} \left(\delta_* - \delta_p\right)^{3/2} f_2^{-3/2}} \quad . \tag{46}$$

By multiplying Eqn. (41) with β, as given in Eqn. (45), the new unloading force relation reads

$$\begin{aligned} F_{n,\mathrm{UL}} &= \frac{4}{3} E_e \underbrace{\beta \sqrt{R_{e,p}}}_{\sqrt{R_{e,p_{\max}}}} \left(\delta_n - \delta_p\right)^{3/2} f_2^{-3/2}, \quad \delta_n \geq \delta_p \\ F_{n,\mathrm{UL}} &= 0, \qquad\qquad\qquad\qquad\quad \delta_n < \delta_p \quad . \end{aligned} \tag{47}$$

To ensure complete unloading from point D to the same point E, δ_p in Eqn. (47) must not change and is still defined by Eqn. (34). Thus, the only variable quantity in Eqn. (47) is the effective plastic contact radius $R_{e,p}$. By defining the modified effective plastic contact radius $R_{e,p_{\max}}$ as

$$R_{e,p_{\max}} = \beta^2 R_{e,p} \quad , \tag{48}$$

we finally get the compact force formulation for the unloading case as

$$\boxed{\begin{aligned} F_{n,\mathrm{UL}} &= \frac{4}{3} E_e \sqrt{R_{e,p_{\max}}} \left(\delta_n - \delta_p\right)^{3/2} f_2^{-3/2}, \quad \delta_n \geq \delta_p \\ F_{n,\mathrm{UL}} &= 0 \qquad\qquad\qquad\qquad\quad , \quad \delta_n \geq \delta_p \end{aligned}} \quad , \tag{49}$$

which is illustrated in Fig. 7.

To conclude, it has to be mentioned, that the demand of continuity of the contact force in point D leads to a sudden jump increase of the contact radius in this point. This fact does neither influence the stability of the DEM solution nor changes the mechanical response of the system and is thus negligible at this point. How to deal with this fact will be content of future work.

4 Finite-Element-Analysis

To validate the theoretical model and to estimate the necessary parameters, FEAs are performed for the contact of two elastic-ideal plastic ellipsoids using ABAQUS [48]. The ABAQUS STANDARD/EXPLICIT finite-element-module uses a solution technology which is suitable for static, low-speed and brief transient dynamic events, which require high accuracy in the stress solutions.

In the mechanical model, shown in Fig. 8, two initially in a single point touching ellipsoids are compressed in normal direction. The contact condition is set to HARD-CONTACT and frictionless in tangential direction. The contact property is chosen to be of type GENERAL CONTACT. The elements are of type C3D10, i.e. ten node tetrahedral elements with quadratic ansatz functions for three dimensional stress states. With respect to the symmetry of the particles, it is sufficient to consider one eighth of each body, only. In the symmetry planes perpendicular to the y and z axes, symmetric boundary conditions are set.

The mesh is refined in the contact zone to better resolve the contact process. Thus, an element size of 10 % of the maximum semi-axis is chosen for the edges in the symmetry planes perpendicular to the x axis, which decreases to a value of 0.5 percent of the smallest semi-axis, when reaching

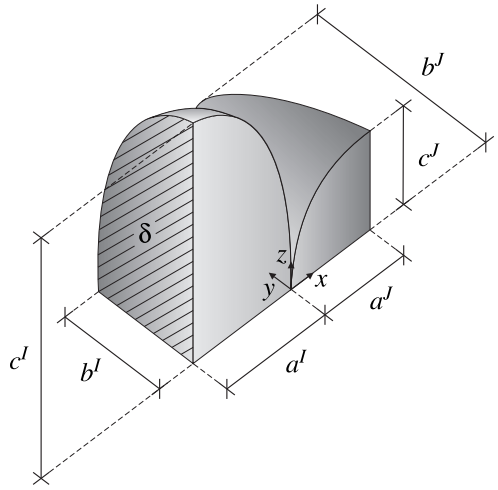

Fig. 8. Sketch of FEM model geometry with semi-axes a^k, b^k, c^k, $k = I, J$ and displacement δ

the contact point. The initially touching ellipsoids are compressed in x-direction displacement driven up to a value of 15 % of the mean radius $\hat{r}^{I,J}$, which is defined as

$$\begin{aligned} \hat{r}^{I,J} &= \hat{r}^I + \hat{r}^J \\ \hat{r}^k &= \left[a^k b^k c^k\right]^{1/3}, \quad k = I, J \quad . \end{aligned} \tag{50}$$

As material parameter set NMC properties are chosen according to [3] and listed in Tab. 1. 25 different cases with

Table 1. Materialparameter for NMC

variable	value	unit
equivalent radius $\hat{r}^k$	$\in [1, 10]$	$[\mu m]$
Young's modulus E	142000	$[MPa]$
Poisson's ratio ν	0.25	$[-]$
density ρ	4750	$[kg/m^3]$
yield strength Y	7900	$[MPa]$
tangent modulus	E/1000	$[-]$

varying aspect ratios of the semi-axes and varying particle sizes are performed, cf. Tab. 2.

Table 2. Case variations of the FE models

$a^k : b^k : c^k$, $k \in [I, J]$	$\hat{r}^k$, $k \in [I, J]$ $[\mu m]$
1 : [0.5..2.0] : [0.5..2.0]	[1.0..10.0]

In Fig. 9, the evolution of the normal contact pressure along the semi-axis a_c of the contact ellipse is plotted. The yellow and the orange line (two left lines) represent the elastic regime, where the maximum contact pressure is $p_0 \leq 1.6Y$ or $a_c/a_Y \leq 1.0$, respectively. The analytical Hertz solution is shown as isolated points, which follow the relation in Eqn. (1). As there is a good agreement, the pressure distribution is well described by Hertz in the elastic regime. Besides, it is obvious, that with further increase of the maximum contact pressure the profile becomes less rounded than the Hertz solution, as can be seen by comparing the light grey points with the light grey curve. Finally, there is a pronounced flattening of the profile resulting in a large region of uniform maximum contact pressure and a sharp pressure drop to zero at the boundary of the contact area. Further normal compression leads to an enlargement of the contact area, only.

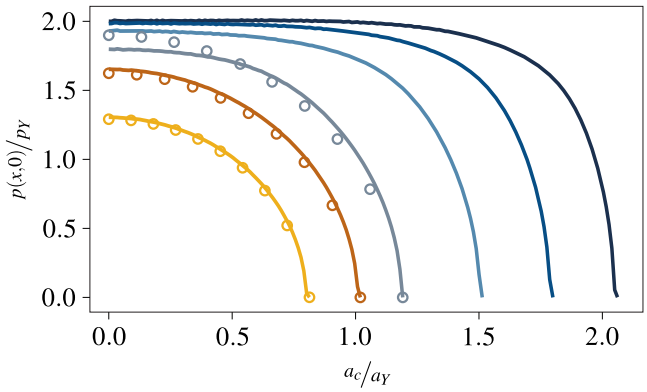

Fig. 9. Normalized contact pressure vs. normalized contact semi-axis in x-direction

As it has been developed in section **3.2**, the maximum contact pressure increases during the elastic-plastic regime further, but slower from $1.6Y$ up to $\lambda_{\max} Y$. In the meantime, the contact radius grows from c_Y up to $\varepsilon_{\max} c_Y$. The values $\lambda_{\max}$ and $\varepsilon_{\max}$ have to be determined according to the results of the FEAs. To find the profile of λ and the related maximum value of $\lambda_{\max}$, the information of the contact force is taken from the FEAs, plotted as dots in Fig. 10. The force, received from the FEA F_{FEM} has to match the force calculated based on the developed theory in Eqn. (25), which yields to the condition

$$F_{\text{FEM}} \stackrel{!}{=} \pi \lambda_{\text{FEM}} Y \left[c_c^2 - c_Y^2\right] + F_{p_Y} \quad . \tag{51}$$

Solving this relation for λ_{FEM}, leads to the profile of λ_{FEM} as shown in Fig. 11. The points represent the FEA result, which is fitted according to Eqn. (28), shown as solid line. $\lambda_{\max}$ is the maximum value of λ_{FEM}, when the plateau in the profile is reached. This belongs to the point, when the maximum contact pressure reaches $p_{\max} = \lambda_{\max} Y$ and the fully plastic similarity regime is entered. From now on, an increase in compression just leads to an enlargement of the contact area, while the maximum contact pressure p_0 remains at the limit value $p_{\max}$. The variable n is set to 1.8 to best fit the profile

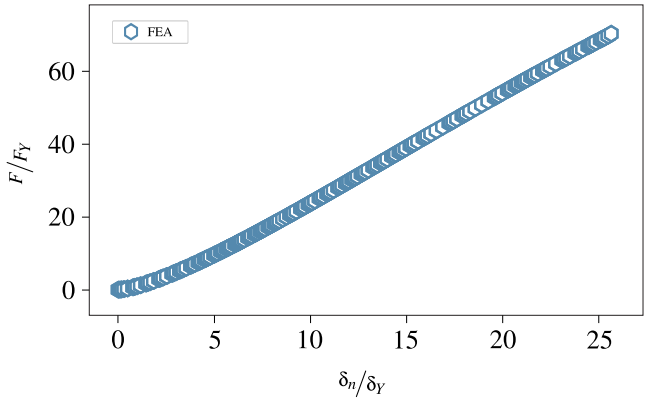

Fig. 10. Normalized contact force vs. normalized displacement, $a^k : b^k : c^k = 1 : 0.66 : 0.66$, $\hat{r}^k = 10.0$, $k = I, J$

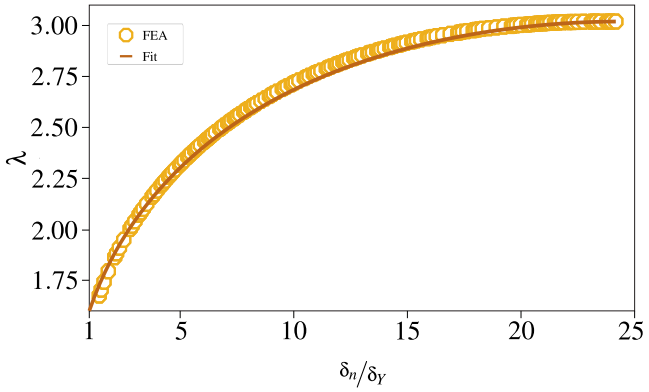

Fig. 11. Evolution of λ vs. normalized displacement, $a^k : b^k : c^k = 1 : 0.66 : 0.66$, $\hat{r}^k = 10.0$, $k = I, J$

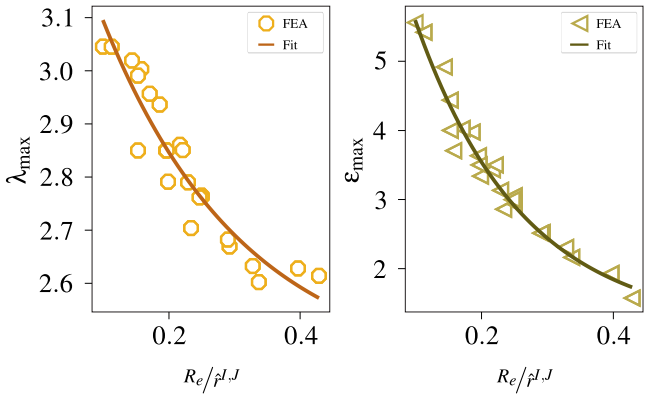

Fig. 12. FEAs and fit for λ_{max} (left) and ε_{max} (right) vs. normalized effective contact radius $R_e/\hat{r}^{I,J}$

of λ. ε_{max} follows as the ratio of the contact radius at λ_{max} to the contact radius at the elastic limit, when $\lambda_Y = 1.6$, as $\varepsilon_{max} = c_{max}/c_Y$.

If λ_{max} and ε_{max} of all 25 different FEA cases are plotted versus the dimensionless effective contact radius $R_e/\hat{r}^{I,J}$, a dependency of both values on the dimensionless effective contact radius is clearly visible.

We take λ_{max} and ε_{max} as fit-functions

$$\begin{aligned} \lambda_{max}\left(R_e, \hat{r}^{I,J}\right) &= m \cdot \exp^{\left\{o \cdot \left[R_e/\hat{r}^{I,J}\right]\right\}} + p \quad , \\ \varepsilon_{max}\left(R_e, \hat{r}^{I,J}\right) &= s \cdot \exp^{\left\{t \cdot \left[R_e/\hat{r}^{I,J}\right]\right\}} + u \quad , \end{aligned} \tag{52}$$

dependent on the dimensionless effective contact radius $R_e/\hat{r}^{I,J}$. Furthermore, m, o, p and s, t, u are fit parameters for which the values

$$\begin{aligned} m = 1.05\,, \quad o = -4.62\,, \quad p = 2.42 \quad , \\ s = 8.19\,, \quad t = -6.14\,, \quad u = 1.14 \quad , \end{aligned} \tag{53}$$

are obtained. The fit-functions follow as

$$\begin{aligned} \lambda_{max}\left(R_e, \hat{r}^{I,J}\right) &= 1.05 \exp^{\left\{-4.62 \cdot \left[R_e/\hat{r}^{I,J}\right]\right\}} + 2.42 \quad , \\ \varepsilon_{max}\left(R_e, \hat{r}^{I,J}\right) &= 8.19 \exp^{\left\{-6.14 \cdot \left[R_e/\hat{r}^{I,J}\right]\right\}} + 1.14 \quad . \end{aligned} \tag{54}$$

5 Validation

In this section, we validate the present model by comparing the model predictions with the results of FEAs. Two selected cases are presented, where the material parameters of NMC are used, which are given in Tab. 1.

In the first selected case, both particles have a mean radius of $\hat{r}^I = \hat{r}^J = 4.675\,\mu m$. The aspect ratios of particle I and J differ and are given in Tab. 3. In a first step, the

Table 3. Aspect ratios of the first selected FEA case

$a^I : b^I : c^I$	$a^J : b^J : c^J$	$\hat{r}^{I,J}$ $[\mu m]$
$1 : 1.25 : 1.5$	$1 : 0.5 : 0.8$	9.35

particles are compressed displacement driven up to 4.5 % of the mean particle radius $\hat{r}^{I,J}$ in x-direction. Further, the particles are completely unloaded and then again compressed up to 10 % of the mean particle radius in x-direction. In a last step, the two ellipsoids are unloaded again. In Fig. 13, the normalized overlap is plotted versus the normalized contact force. The normalization is performed with the values at the yield point, which are the overlap δ_Y and the corresponding contact force F_{p_Y}. Thus, if a normalized overlap of $\delta_n/\delta_Y = 1.0$ is exceeded, the elastic-plastic regime is entered. The result of the FEA is plotted with light blue points, while the here developed theory is shown as dark blue solid line. The mean error between the theory prediction and the FEA is low with $\overline{\text{err}} = 1.01\,\%$. The dashed green curve in Fig. 13 represents the model calculation for the contact of two elastoplastic spherical particles, which have the same mean radius of $r^I = r^J = 4.675\,\mu m$, as the two considered ellipsoids. The spherical prediction overestimates the real force-displacement relationship between the two ellipsoidal bodies. Thus, for a realistic description of the acting contact

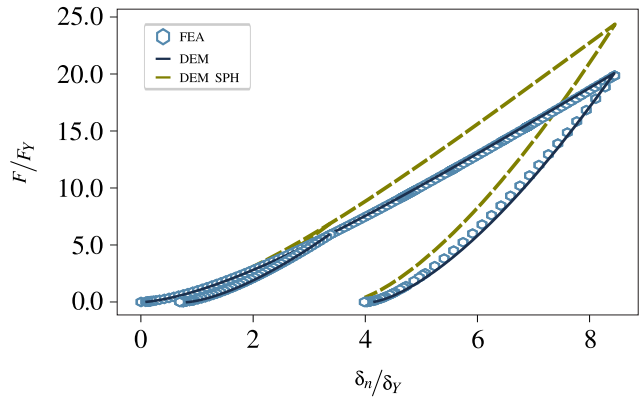

Fig. 13. Normalized contact force vs. normalized displacement: ellipsoids (blue line), spheres (green line), FEA (points)

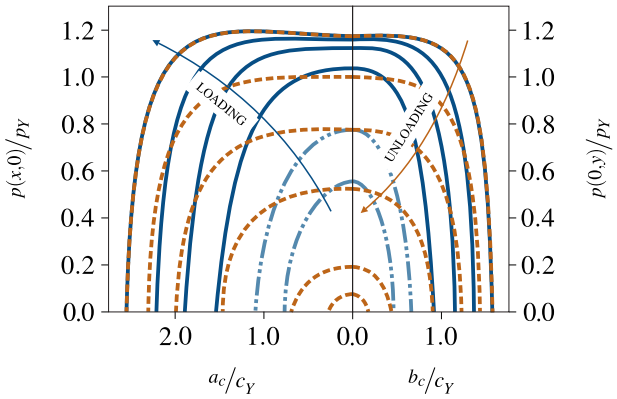

Fig. 14. Normalized contact semi-axes vs. normalized contact pressure: elastic loading (blue dashed-dotted lines), elastic-plastic loading (blue solid lines), unloading (orange dashed lines)

force in dependency of the normal overlap, the theory has to incorporate the shape of the contact zone, as has been done for the present model development.

In Fig. 14, the normalized contact pressure of the first loading and unloading cycle as obtained from FEA is plotted versus the normalized semi-axes of the contact ellipse. The graph is divided in a left and a right part, which share the y-axis, but have different x-axes. In the left part, the x-axis represents the direction of the larger normalized semi-axis a_c/c_Y of the contact ellipse. In the right part, the x-axis coincides with the direction of the smaller normalized semi-axis b_c/c_Y. We normalize the semi-axes with the equivalent contact radius at the yield point c_Y to emphasize the eccentricity of the contact area. It is evident from comparing the scales of both x-axes, that the contact area is elliptical. In the contact configuration simulated here, there is no relative sliding in the contact area. Therefore, the eccentricity of the contact ellipse, which is governed by the principle curvatures in the contact point, which in turn depend on the semi-axes of the contacting ellipsoids and their mean radius, stays constant during the whole contact history and happens to be $e = 0.65$ in the current case. The blue curves represent the loading stage, while the orange dashed curves show the pressure distribution during unloading. Concerning the blue curves, a subdivision in the elastic (Hertzian) regime and the elastic-plastic regime can be done. The light blue dashed-dotted curves represent the elastic regime. The elastic-plastic regime is plotted as solid dark blue lines. It is visible that with increasing maximum contact pressure, corresponding to an increasing displacement, the contact pressure profile flattens more and more. In the point of return, where the loading pressure distribution equals the unloading pressure distribution, which means that the solid blue curve and the dashed orange curve lie exactly over each other, already a large almost flat area has formed. During unloading the pressure distribution recedes slowly, until it finally has again a parabolic profile. At separation the contact area runs to zero. These observations clearly confirm the assumptions made for the derivation of the contact law with an elastic-plastic and a fully plastic regime.

In the second case, both particles have the same mean radius of $\hat{r}^I = \hat{r}^J = 10.0\,\mu m$, but different aspect ratios, given in Tab. 4. Firstly, the particles are compressed displacement driven up to 10 % of the mean particle radius $\hat{r}^{I,J}$ in x-direction. Subsequently, the particles are completely unloaded, before reloaded by applying a maximum displacement of 13 % of the mean particle radius in x-direction. Finally, the two ellipsoids are unloaded again. In Fig. 15, the normalized overlap is plotted versus the normalized contact force, by means of the same normalization ansatz as in Fig. 13. For values of the normalized overlap larger than $\delta_n/\delta_Y = 1.0$, the contact behavior is in the elastic-plastic regime. As a value of $\varepsilon_{\max} = 2.94$ can be obtained for the current contact situation, the fully plastic similarity regime is reached, when the normalized overlap is larger than $\delta_n/\delta_Y = 8.65$. The theory prediction in Fig. 15 is shown as solid dark blue line, while the FEA is plotted as isolated light blue points. Both results agree very well. The mean error is with $\overline{\text{err}} = 0.59\,\%$ very low. As comparison, the prediction with the elastic - fully plastic theory, shown as dashed yellow line, is added. It is obvious, that the theory without incorporating the elastic-plastic transition regime, significantly underestimates the acting contact force. Thus, it is indispensable to provide a theory formulation, which includes the elastic-plastic transition regime.

Table 4. Aspect ratios of the second selected FEA case

$a^I : b^I : c^I$	$a^J : b^J : c^J$	$\hat{r}^{I,J}$ [μm]
1 : 1 : 0.8	1 : 1.25 : 1.25	20.0

The overall good agreement between FEAs and the predictions of the here developed model, for both, the loading and the unloading case, confirm the present model.

6 Conclusions

In this paper, a theoretical model for the normal contact force of two elastoplastic ellipsoidal bodies having aspect ra-

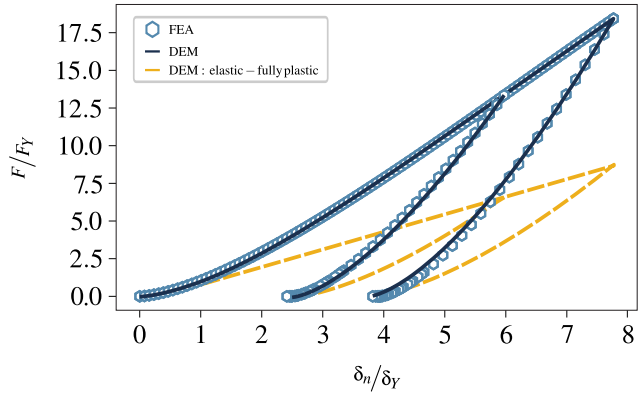

Fig. 15. Normalized contact force vs. normalized displacement: elastic - plastic theory (yellow line), elastic - elastic-plastic - fully plastic theory (blue line), FEA (points)

tios in the range of $a^k : b^k : c^k = 1 : [0.5..2.0] : [0.5..2.0]$, $k = I, J$ is presented. All necessary formulae to describe the contact force-displacement relationship are derived. Finite-Element-Analyses of the static compression between two elastic-ideal plastic ellipsoidal bodies are performed, in order to estimate all necessary parameters for the fit in the elastic-plastic transition regime and to validate the present model. It has to be mentioned that the relationships in the elastic and in the fully plastic similarity regime are universally valid for ellipsoidal bodies and independent of the present material, while the fit in the elastic-plastic transition regime is developed for lithium nickel manganese cobalt oxide material and may slightly change for other material properties. As a good agreement is obtained comparing the FEA results and the predictions of the present model for both loading and unloading, the validation of the present model is successfully demonstrated.

Acknowledgements

This work has been supported by the German Research Foundation (DFG) in the framework of the SiMET research training group (GRK 2218). Furthermore, this work contributes to the research performed at CELEST (Center for Electrochemical Energy Storage Ulm-Karlsruhe).

References

[1] Cundall, P., and Strack, O., 1979. "A discrete numerical model for granular assemblies". *Géotechnique,* **29**(1), pp. 47 – 65.

[2] Cheng, E. J., Hong, K., Taylor, N. J., Choe, H., Wolfenstine, J., and Sakamoto, J., 2017. "Mechanical and physical properties of $LiNi_{0.33}Mn_{0.3}Co_{0.33}O_2$ (NMC)". *Journal of the European Ceramic Society,* **37**(9), aug, pp. 3213–3217.

[3] Giménez, C. S., Finke, B., Schilde, C., Froböse, L., and Kwade, A., 2019. "Numerical simulation of the behavior of lithium-ion battery electrodes during the calendaring process via the discrete element method". *Powder Technology,* **349**, may, pp. 1–11.

[4] Ott, J., Völker, B., Gan, Y., McMeeking, R. M., and Kamlah, M., 2013. "A micromechanical model for effective conductivity in granular electrode structures". *Acta Mechanica Sinica,* **29**(5), oct, pp. 682–698.

[5] Antartis, D., Dillon, S., and Chasiotis, I., 2015. "Effect of porosity on electrochemical and mechanical properties of composite li-ion anodes". *Journal of Composite Materials,* **49**(15), jan, pp. 1849–1862.

[6] Zheng, H., Tan, L., Liu, G., Song, X., and Battaglia, V. S., 2012. "Calendering effects on the physical and electrochemical properties of $Li[Ni_{1/3}Mn_{1/3}Co_{1/3}]O_2$ cathode". *Journal of Power Sources,* **208**, jun, pp. 52–57.

[7] Haselrieder, W., Ivanov, S., Christen, D. K., Bockholt, H., and Kwade, A., 2013. "Impact of the calendering process on the interfacial structure and the related electrochemical performance of secondary lithium-ion batteries". *ECS Transactions,* **50**(26), apr, pp. 59–70.

[8] Schmidt, D., Kamlah, M., and Knoblauch, V., 2018. "Highly densified NCM-cathodes for high energy li-ion batteries: Microstructural evolution during densification and its influence on the performance of the electrodes". *Journal of Energy Storage,* **17**, jun, pp. 213–223.

[9] Schmidt, D., Kleinbach, M., Kamlah, M., and Knoblauch, V., 2018. "Investigations on the microstructure-property relationship of NCM-based electrodes for lithium-ion batteries". *Practical Metallography,* **55**(11), nov, pp. 741–761.

[10] Hertz, H., 1881. "Über die Berührung fester elastischer Körper". *Journal für die reine und angewandte Mathematik,* **92**, pp. 156–171.

[11] Thakur, S. C., Morrissey, J. P., Sun, J., Chen, J. F., and Ooi, J. Y., 2014. "Micromechanical analysis of cohesive granular materials using the discrete element method with an adhesive elasto-plastic contact model". *Granular Matter,* **16**(3), may, pp. 383–400.

[12] Pasha, M., Dogbe, S., Hare, C., Hassanpour, A., and Ghadiri, M., 2014. "A linear model of elasto-plastic and adhesive contact deformation". *Granular Matter,* **16**(1), jan, pp. 151–162.

[13] Walton, O. R., and Braun, R. L., 1986. "Viscosity, granular-temperature, and stress calculations for shearing assemblies of inelastic, frictional disks". *Journal of Rheology,* **30**(5), oct, pp. 949–980.

[14] Luding, S., 2008. "Cohesive, frictional powders: contact models for tension". *Granular Matter,* **10**(4), mar, pp. 235–246.

[15] Vu-Quoc, L., and Zhang, X., 1999. "An elastoplastic contact force–displacement model in the normal direction: displacement–driven version". *Proceedings of the Royal Society of London. Series A: Mathematical, Physical and Engineering Sciences,* **455**(1991), nov, pp. 4013–4044.

[16] Müller, P., and Tomas, J., 2012. "Compression behavior of moist spherical zeolite 4a granules". *Chemical*

Engineering & Technology, **35**(9), aug, pp. 1677–1684.

[17] Hardy, C., Baronet, C. N., and Tordion, G. V., 1971. "The elasto-plastic indentation of a half-space by a rigid sphere". *International Journal for Numerical Methods in Engineering,* **3**(4), oct, pp. 451–462.

[18] Mesarovic, S. D., and Fleck, N. A., 1999. "Spherical indentation of elastic–plastic solids". *Proceedings of the Royal Society of London. Series A: Mathematical, Physical and Engineering Sciences,* **455**(1987), jul, pp. 2707–2728.

[19] Sinclair, G., Follansbee, P., and Johnson, K., 1985. "Quasi-static normal indentation of an elasto-plastic half-space by a rigid sphere—II. results". *International Journal of Solids and Structures,* **21**(8), pp. 865–888.

[20] Follansbee, P., and Sinclair, G., 1984. "Quasi-static normal indentation of an elasto-plastic half-space by a rigid sphere—I: Analysis". *International Journal of Solids and Structures,* **20**(1), pp. 81–91.

[21] Hill, R., Storåkers, B., and Zdunek, A. B., 1989. "A theoretical study of the brinell hardness test". *Proceedings of the Royal Society of London. A. Mathematical and Physical Sciences,* **423**(1865), jun, pp. 301–330.

[22] Kral, E. R., Komvopoulos, K., and Bogy, D. B., 1993. "Elastic-plastic finite element analysis of repeated indentation of a half-space by a rigid sphere". *Journal of Applied Mechanics,* **60**(4), dec, pp. 829–841.

[23] Yu, M., Moran, B., and Keer, L. M., 1993. "A direct analysis of two-dimensional elastic-plastic rolling contact". *Journal of Tribology,* **115**(2), apr, pp. 227–236.

[24] Yu, M. M.-H., Moran, B., and Keer, L. M., 1995. "A direct analysis of three-dimensional elastic-plastic rolling contact". *Journal of Tribology,* **117**(2), apr, pp. 234–243.

[25] Kogut, L., and Etsion, I., 2002. "Elastic-plastic contact analysis of a sphere and a rigid flat". *Journal of Applied Mechanics,* **69**(5), aug, pp. 657–662.

[26] Jackson, R. L., and Green, I., 2005. "A finite element study of elasto-plastic hemispherical contact against a rigid flat". *Journal of Tribology,* **127**(2), apr, pp. 343–354.

[27] Thornton, C., Cummins, S. J., and Cleary, P. W., 2017. "On elastic-plastic normal contact force models, with and without adhesion". *Powder Technology,* **315**, jun, pp. 339–346.

[28] Mesarovic, S. D., and Fleck, N. A., 2000. "Frictionless indentation of dissimilar elastic–plastic spheres". *International Journal of Solids and Structures,* **37**(46-47), nov, pp. 7071–7091.

[29] Thornton, C., 1997. "Coefficient of restitution for collinear collisions of elastic-perfectly plastic spheres". *Journal of Applied Mechanics,* **64**(2), jun, pp. 383–386.

[30] Martin, C., 2003. "Unloading of powder compacts and their resulting tensile strength". *Acta Materialia,* **51**(15), sep, pp. 4589–4602.

[31] Thornton, C., and Ning, Z., 1998. "A theoretical model for the stick/bounce behaviour of adhesive, elastic-plastic spheres". *Powder Technology,* **99**(2), sep, pp. 154–162.

[32] Tabor, D., 1951. *Hardness of Metals*. Oxford University Press.

[33] Li, L., Wu, C., and Thornton, C., 2001. "A theoretical model for the contact of elastoplastic bodies". *Proceedings of the Institution of Mechanical Engineers, Part C: Journal of Mechanical Engineering Science,* **216**(4), apr, pp. 421–431.

[34] Chung, J. C., 2010. "Elastic–plastic contact analysis of an ellipsoid and a rigid flat". *Tribology International,* **43**(1-2), jan, pp. 491–502.

[35] Lin, L. P., and Lin, J. F., 2007. "An elliptical elastic-plastic microcontact model developed for an ellipsoid in contact with a smooth rigid flat". *Journal of Tribology,* **129**(4), jun, pp. 772–782.

[36] Jeng, Y.-R., and Wang, P.-Y., 2003. "An elliptical microcontact model considering elastic, elastoplastic, and plastic deformation". *Journal of Tribology,* **125**(2), mar, pp. 232–240.

[37] Jamari, J., and Schipper, D. J., 2006. "An elastic–plastic contact model of ellipsoid bodies". *Tribology Letters,* **21**(3), mar, pp. 262–271.

[38] Jamari, J., and Schipper, D., 2007. "Plastic deformation and contact area of an elastic–plastic contact of ellipsoid bodies after unloading". *Tribology International,* **40**(8), aug, pp. 1311–1318.

[39] Horng, J. H., 1998. "An elliptic elastic-plastic asperity microcontact model for rough surfaces". *Journal of Tribology,* **120**(1), jan, pp. 82–88.

[40] Reussner, H., 1977. "Druckflächenbelastung und Oberflächenverschiebung im Wälzkontakt von Rotationskörpen". PhD thesis, University of Karlsruhe.

[41] Moes, H. Lubrication and beyond. University of Twente Lecture Notes code 115531.

[42] Johnson, K., 1985. *Contact Mechanics*. Cambridge University Press.

[43] Hale, L. C., 1999. "Principles and techniques for designing precision machines". PhD thesis, University of California.

[44] Ghaednia, H., Wang, X., Saha, S., Xu, Y., Sharma, A., and Jackson, R. L., 2017. "A review of elastic–plastic contact mechanics". *Applied Mechanics Reviews,* **69**(6), nov.

[45] Harris, W. F., 2006. "Curvature of ellipsoids and other surfaces". *Ophthalmic and Physiological Optics,* **26**(5), sep, pp. 497–501.

[46] Wu, C., Li, L., and Thornton, C., 2003. "Rebound behaviour of spheres for plastic impacts". *International Journal of Impact Engineering,* **28**(9), oct, pp. 929–946.

[47] Bower, A. F., Fleck, N. A., Needleman, A., and Ogbonna, N., 1993. "Indentation of a power law creeping solid". *Proceedings of the Royal Society A: Mathematical, Physical and Engineering Sciences,* **441**(1911), apr, pp. 97–124.

[48] Simulia, D. S., 2012. "Abaqus 6.12 documentation". *Providence, Rhode Island, US,* **261**.

[49] Struik, D. J., 1922. *Grundzüge der Mehrdimensionalen Differentialgeometrie*. Springer Berlin Heidelberg.

Appendix A: Calculation of the contact geometry of ellipsoidal bodies

In this appendix, all necessary information to describe the geometry of an ellipsoidal body in any point of its surface is presented. The derivation follows the approach of Harris [45], where a more detailed description can be found.

First of all, a transformation from the global coordinate system into the local body system of each ellipsoid is useful, where the origin of the body system is located in the center of the ellipsoid with the three major axis along the semi-axis a, b and c. Doing so simplifies the description of the ellipsoidal surface and thus the derivation of the formulae to calculate the maximum and the minimum curvature in any point of the surface.

In the body system, the principal curvature and the belonging directions are searched. Starting with the implicit equation

$$\frac{x^2}{a^2}+\frac{y^2}{b^2}+\frac{z^2}{c^2}=1 \tag{55}$$

of an ellipsoid, one may solve the equation with respect to x, y or z. Solving, for example, for x gives

$$x=a\sqrt{1-\frac{y^2}{b^2}-\frac{z^2}{c^2}} \quad , \tag{56}$$

where due to symmetry only the positive part of the root of x has to be considered. Any random point $\mathbf{x}$ at the surface of the ellipsoid has the position vector

$$\mathbf{x}=\left[a\sqrt{1-\frac{y^2}{b^2}-\frac{z^2}{c^2}},y,z\right]^T \quad . \tag{57}$$

Equation (57) is a parametric representation of an ellipsoid. The first and second spacial derivatives are

$$\begin{aligned}
\frac{\partial \mathbf{x}}{\partial y}&=\left[-\frac{a^2 y}{b^2 x},1,0\right]^T \quad ,\\
\frac{\partial \mathbf{x}}{\partial z}&=\left[-\frac{a^2 z}{c^2 x},0,1\right]^T \quad ,\\
\frac{\partial^2 \mathbf{x}}{\partial y^2}&=\left[-\frac{a^2}{b^2 x}\left(1+\frac{a^2 y^2}{b^2 x^2}\right),0,0\right]^T \quad ,\\
\frac{\partial^2 \mathbf{x}}{\partial y \partial z}&=\left[-\frac{a^4 yz}{b^2 c^2 x^3},0,0\right]^T \quad ,\\
\frac{\partial^2 \mathbf{x}}{\partial z^2}&=\left[-\frac{a^2 z}{c^2 x}\left(1+\frac{a^2 z^2}{c^2 x^2}\right),0,0\right] \quad .
\end{aligned} \tag{58}$$

For the normal vector $\mathbf{n}$, it follows

$$\mathbf{n}=\left[1,\frac{a^2 y}{b^2 x},\frac{a^2 z}{c^2 x}\right]^T \quad , \tag{59}$$

with its length n

$$n=\sqrt{1+\frac{a^4 y^2}{b^4 x^2}+\frac{a^4 z^2}{c^4 x^2}} \quad . \tag{60}$$

The so-called first fundamental form, representing the *inner geometry* of a surface, is described by the coefficients E, F and G, which can be calculated as

$$E=\frac{a^4 y^2}{b^4 x^2}+1\,, \quad F=\frac{a^4 yz}{b^2 c^2 x^2}\,, \quad G=\frac{a^4 z^2}{c^4 x^2}+1 \quad . \tag{61}$$

The inner geometry describes geometrical quantities, such as the distance of two points at the surface or the computation of a selected part of the surface area [49]. For the second fundamental form, which gives the properties of the *outer geometry*, the coefficients L, M and N are defined by

$$L=\frac{a^4\left(c^2-z^2\right)}{b^2 c^2 n x^3}\,, \quad M=\frac{a^4 yz}{b^2 c^2 n x^3}\,, \quad N=\frac{a^4\left(b^2-y^2\right)}{b^2 c^2 n x^3} \quad . \tag{62}$$

The outer geometry describes the position of the surface in the surrounding space [49]. Finally, the principal curvature values κ_1, κ_2 in point $\mathbf{x}$ are determined using the first and second fundamental form according to [49] as

$$\kappa_{1,2}=\frac{L\cos^2\theta+2M\cos\theta\sin\theta+N\sin^2\theta}{E\cos^2\theta+2F\cos\theta\sin\theta+G\sin^2\theta} \quad . \tag{63}$$

In any point at the surface, the curvature usually depends on the direction. The corresponding angles θ to the two principal curvatures κ are given by the solutions of

$$\begin{aligned}
&(EM-FL)\cos^2\theta+(EM-GL)\\
&\qquad\cos\theta\sin\theta+(FN-GM)\sin^2\theta=0 \quad .
\end{aligned} \tag{64}$$

If $\theta\neq 0$, it follows

$$(EM-FL)\frac{1}{\tan^2\theta}+(EM-GL)\frac{1}{\tan\theta}+(FN-GM)=0 \tag{65}$$

and using the substitution $\dfrac{1}{\tan\theta}=s$,

$$(EM-FL)s^2+(EM-GL)s+(FN-GM)=0 \quad . \tag{66}$$

There are two solutions for s

$$s_{1,2} = \frac{-(EM-GL) \pm \sqrt{(EM-GL)^2 - 4(EM-FL)(FN-GM)}}{2(EM-FL)} \quad , \tag{67}$$

which gives

$$\theta_{1,2} = \arctan \frac{1}{s_{1,2}} \quad . \tag{68}$$

The principal curvature directions $\mathbf{K}_1, \mathbf{K}_2$ follow as

$$\mathbf{K}_{1,2} = \cos\theta_{1,2} \begin{bmatrix} -\frac{a^2 y}{b^2 x} \\ 1 \\ 0 \end{bmatrix} + \sin\theta_{1,2} \begin{bmatrix} -\frac{a^2 z}{c^2 x} \\ 0 \\ 1 \end{bmatrix} \quad . \tag{69}$$

Finally, when all the above calculated information is known in the contact point of two ellipsoidal bodies, the angle of inclination α is computed by

$$\cos\alpha = \frac{\mathbf{K}_1^I \cdot \mathbf{K}_1^J}{|\mathbf{K}_1^I|\,|\mathbf{K}_1^J|} = \frac{\mathbf{K}_2^I \cdot \mathbf{K}_2^J}{|\mathbf{K}_2^I|\,|\mathbf{K}_2^J|} \quad . \tag{70}$$

Appendix B: Calculation of the contact stiffness

In this appendix, the derivation of the plastic contact stiffness, as well as the Hertzian contact stiffness is presented. The plastic contact stiffness is given as the derivation of the plastic contact force F_N with respect to the normal overlap δ_n as

$$\begin{aligned} \frac{\partial F_n}{\partial \delta_n} = k_{n,p_Y} &= \frac{\partial \left[\pi p_Y \left(\underbrace{\delta_n R_e \frac{f_1^2}{f_2}}_{c_c^2} - c_Y^2 \right) + \frac{4}{3} E_e \sqrt{R_e} \delta_Y^{3/2} f_2^{-3/2} \right]}{\partial \delta_n} \\ &= \pi R_e \frac{f_1^2}{f_2} p_Y \quad . \end{aligned} \tag{71}$$

For the Hertzian contact stiffness, the elastic Hertzian force F_H is derived with respect to the normal overlap δ_n. It follows

$$\begin{aligned} \frac{\partial F_H}{\partial \delta_n} = k_{H,\delta_n} &= \frac{\partial \left[\frac{4}{3} E_e \sqrt{R_e} \delta_n^{3/2} f_2^{-3/2} \right]}{\partial \delta_n} \\ &= \frac{2 E_e \sqrt{R_e} \sqrt{\delta_n}}{f_2^{3/2}} \quad . \end{aligned} \tag{72}$$